ENVIRONMENTAL RESEARCH
LETTERS

OPEN ACCESS

RECEIVED
17 September 2020

REVISED
23 January 2021

ACCEPTED FOR PUBLICATION
8 February 2021

PUBLISHED
22 February 2021

LETTER

Tropical African wildfire aerosols trigger teleconnections over mid-to-high latitudes of Northern Hemisphere in January

Huiping Yan[1], Zhiwei Zhu[1,2], Bin Wang[1,3], Kai Zhang[4], Jingjia Luo[1], Yun Qian[4] and Yiquan Jiang[5]

[1] School of Atmospheric Sciences, Nanjing University of Information Science and Technology, Nanjing, People's Republic of China
[2] State Key Laboratory of Numerical Modeling for Atmospheric Sciences and Geophysical Fluid Dynamics, Institute of Atmospheric Physics, Chinese Academy of Sciences, Beijing, People's Republic of China
[3] Department of Meteorology, University of Hawaii at Manoa, Honolulu, HI, United States of America
[4] Pacific Northwest National Laboratory, Richland, WA, United States of America
[5] School of Atmospheric Sciences, Nanjing University, Nanjing, People's Republic of China

E-mail: zwz@nuist.edu.cn

Keywords: African wildfire aerosol, teleconnection, black carbon, Europe land surface warming

Supplementary material for this article is available online

Abstract

This study investigates the impacts of African wildfire aerosols (primary organic carbon, black carbon and sulfate) on the Northern Hemispheric in January. We found that wildfire aerosols emitted from equatorial Africa result in two mid-to-high latitudes atmospheric Rossby wave trains. One is from subtropical Atlantic propagating northeastward across Europe to Siberia, and the other one propagates eastward from Middle East across Asia to Pacific Northwest. The maximum positive geopotential height anomaly locates in Europe, concurrent with a greater-than-2 K land surface warming. These Rossby wave trains are excited by the atmospheric heating that caused by the wildfire aerosols in equatorial Africa and propagate into extratropics with the help of the westerly jet. Based on the diabatic heat budget analysis, the Rossby wave source is primarily from the solar absorption of black carbon of African wildfire. The present study emphasizes that wildfire aerosols, especial the absorbing aerosols, would have profound climate effects on remote regions and thus need more attentions.

1. Introduction

Aerosol through scattering and absorbing solar radiation could alter energy balance, and also can be activated as cloud droplet nuclei or ice nuclei, changing cloud microphysical properties and affecting cloud radiative effects. Although the aerosol radiative effects and aerosol–cloud interactions have been widely studied and evaluated, they are still long-lasting hot topics in the atmospheric community. The radiative forcing of aerosols could induce regional warming or cooling (e.g. Ramanathan and Carmichael 2008, Chen *et al* 2016, Li *et al* 2016), and the persistence of the regional anomalies could further induce large-scale climate response via dynamic or thermodynamic processes.

Great efforts have been devoted to investigating the regulation of aerosol effects on regional climate. For example, the deposition of dust and black carbon (BC) on Tibetan Plateau could amplify the heat pump effect, which would advance the onset of South Asian monsoon, and affect East Asia monsoon (Lau *et al* 2006). BC emitted over India could advance the Indian monsoon onset (Bollasina *et al* 2013), leading to increased (suppressed) pre-monsoon (monsoon) rainfall (Ganguly *et al* 2012) through absorbing solar radiation and increasing the meridional temperature gradient (Meehl *et al* 2008). The impacts of anthropogenic aerosols on East Asian monsoon has been also studied widely (Qian *et al* 2001, Giorgi *et al* 2002, 2003, Liu *et al* 2009, Zhang *et al* 2012, Jiang *et al* 2013, Song *et al* 2014, Li *et al* 2016). A more recent atmosphere-ocean coupled modeling study (Lou *et al* 2019) showed that BC heating over North China can weaken East Asian winter monsoon through changing land–sea thermal contrast and cloud feedbacks. In addition, polluted snow with light-absorbing aerosols over Tibetan Plateau could decrease snow albedo, leading to reduced snow cover that in turn changes

the East Asian climates (Qian *et al* 2011, Yasunari *et al* 2015).

Aerosols not only exert local climate impacts on surrounding regions (Yang *et al* 2018, Zhou *et al* 2020), but also generate global impacts, such as weakening the Hadley Cell (Allen and Sherwood 2011, Tosca *et al* 2013), and shifting the subtropical westerly jets (Ming *et al* 2011). A few works have reported that teleconnections may be induced by aerosols. Rodwell and Jung (2008) suggested the role of Sahara dust in driving the planetary waves. Kim *et al* (2006) reported that the direct radiative effects of dust and BC could excite a planetary wave spanning from North Africa through Eurasia to the North Pacific in boreal spring. However, these two studies only considering the absorbing aerosols. What are the global circulation responses when scattering aerosols and the indirect radiative effects of aerosols are also involved? This is an interesting issue merits further investigation.

This work is a follow-up study of Jiang *et al* (2016) in which the direct and indirect effects of three types of fire aerosols (sulfate, BC, and primary organic matter) are investigated. The indirect effects of fire aerosol are found to be much larger than its direct effects. With the basic understanding of the thermodynamic properties of Africa wildfire aerosols, in the present study we aim to unravel how the remote climate responses (the teleconnections) of aerosols are established via numerical simulations. The reasons for choosing January as the target study period are two folds. First, the African wildfire mostly occur in boreal winter with the peak in January. Second, given that North Africa is the only major wildfire source on the earth during January, it is a time window to identify the remote climate impacts of biomass burning aerosols. The remainder of this paper is organized as follows. Section 2 introduces the overview of model and experiments. Section 3 presents the radiative effects of the Africa wildfire aerosols and corresponding circulation changes, and explores the cause of the atmospheric teleconnections. The conclusion and discussion are provided in section 4.

2. Model and experiment design

2.1. Model

The Community Atmosphere Model version 5.3 (CAM5.3) (Neale *et al* 2010) with the finite volume dynamics core are used. A two-moment cloud microphysics scheme (Morrison *et al* 2008) is adopted in the model. The Modal Aerosol Model (MAM4) that consists of four lognormal modes (Aitken, accumulation, coarse, and primary carbon mode) is used to predict aerosol mass and number mixing ratios (Liu *et al* 2016). The primary carbon mode is included to improve the treatment of microphysical ageing of BC and POM (Liu *et al* 2016).

Table 1. The descriptions of CAM5 experiments in this study.

Name	Experiment configuration
noFire	AR5 emission data
Fire	AR5 emission data plus GFED (BC, POM, SO_x)
noBC	AR5 emission data plus GFED (POM, SO_x)

2.2. Experiment design

As listed in the table 1, three experiments were conducted to investigate the climate impacts of wildfire aerosols. The first is the control experiment which is performed without fire aerosols (named as noFire experiment). The second one is the sensitivity experiment which is run with fire aerosols (named as Fire experiment). The third experiment (noBC experiment) was conducted with fire BC emissions turned off to distinguish the effects of absorbing aerosols from the total effects. Daily fire emissions of BC, POM and sulfur dioxide (SO_2) during January from the Global Fire Emissions Database version 3.1 (GFED 3.1) (Giglio *et al* 2013) are prescribed in Fire and noBC experiments. Anthropogenic aerosol and precursor gas emissions from the IPCC AR5 dataset (AR5 emission, Lamarque *et al* 2010) are employed in both Fire and noFire experiments. Historical sea surface temperature and sea ice are prescribed in the model. Simulations were carried out from 2003 to 2011 with a horizontal resolution of $0.9° \times 1.25°$ and 30 vertical layers. The climate responses to the African wildfire aerosols were derived as the differences between Fire/noBC and noFire experiments. A local t test was applied to judge the statistical significance of the differences between the control run and sensitivity run (Zhu *et al* 2014). The detailed descriptions of simulations and analysis of the aerosol radiative effects can be found in Jiang *et al* (2016).

3. Results

Boreal winter is the fire season over North Africa (van der Werf *et al* 2017), and the wildfire mostly occur in January with its carbon emissions up to 160 Tg C per month (see the supplementary material figure S1, which is available online at stacks.iop.org/ERL/16/034025/mmedia). At that time, Africa is the major fire hotspot (figure 1(a)). Considering the lifetime of wildfire aerosols in troposphere is from several days to 2 weeks, the corresponding atmospheric responses are also within the timescale of one month (Jacob 1999). Thus, in the following paper, we only show differences in January between Fire and noFire experiments to illustrate the African wildfire climate impacts. As the aerosols have significant impacts on the radiative budgets, we present the radiative effects as well as the direct and indirect effects in section 3.1, demonstrate the impacts on atmospheric circulation in section 3.2,

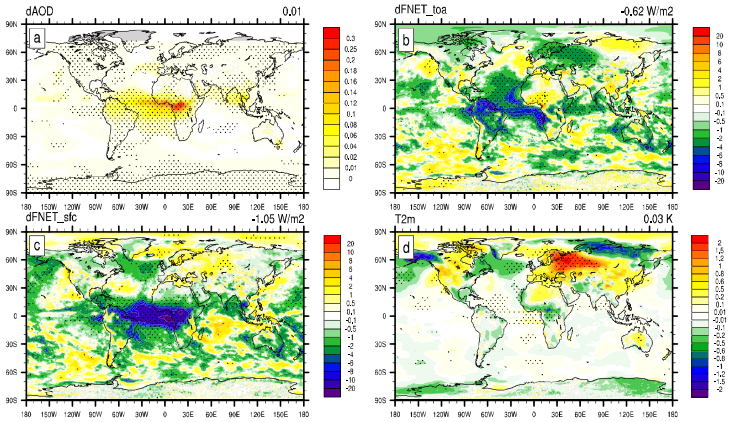

Figure 1. The spatial distribution of the changes in (a) aerosol optical depth (dAOD), the radiative flux (b) at the top of atmosphere (dFNET_toa, W m^{-2}), (c) at surface (dFNET_sfc, W m^{-2}), and (d) air temperature 2 m above the surface (T2m, K) due to wildfire aerosols. The differences passing 95% confidence level are dotted. The value shown in the upper right of each panel is the global average of each variable.

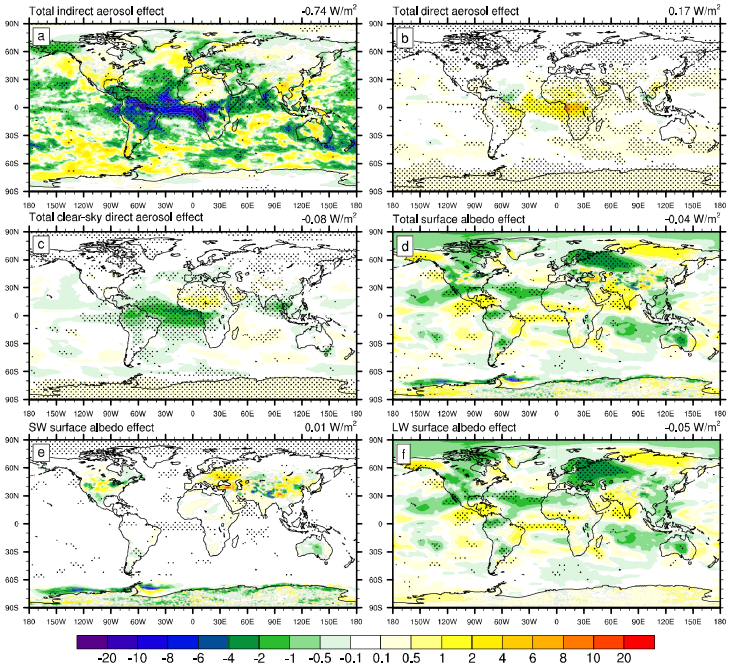

Figure 2. The spatial distribution of (a) total aerosol–cloud interactive effects, (b) total direct radiative effects, (c) total direct radiative effects at clear-sky, (d) total surface albedo effects, (e) the SW surface albedo effects and (f) the LW surface albedo effects (units: W m^{-2}). The differences passing 95% confidence level are dotted. The value shown in the upper right of each panel is the global average of each variable.

and link the aerosols with the circulation anomalies in section 3.3.

3.1. Fire aerosol-induced radiative fluxes

Figure 1 shows the impact of fire aerosols on the aerosol optical depth (AOD), radiative fluxes, and surface temperature. The maximum changes of AOD (dAOD > 0.25) is located in the equatorial Africa and the downstream region of the entire tropical Atlantic (figure 1(a)). The fire aerosol effects on the net radiative flux (FNET) at the top of the atmosphere (dFNET_toa) and at the surface (dFNET_sfc) are shown in figures 1(b) and (c), respectively. The maximum negative dFNET_toa (up to -10 W m^{-2}) is consistent with the maximum increase of AOD over tropical Atlantic. The second maximum negative dFNET_toa (around -2 W m^{-2}) appears over Europe, where the increase of AOD is weak. The dFNET_sfc can be -20 W m^{-2} over the tropical Atlantic. The pronounced difference between dFNET_sfc and dFNET_toa over the equatorial Atlantic implies that the fire aerosol absorption in the atmosphere is quite strong. Significant changes in surface air temperature (figure 1(d)) can be found over mid-to-high latitudes of Europe, Northern Russian, and Alaska. However, the changes in AOD and

FNET_sfc are not significant in these regions, and the negative change in FNET_toa will result in an overall cooling. This suggests that the local changes in radiative fluxes cannot explain the changes in surface air temperature in the regions, especially for the remarkable warming over Europe.

We decompose the total aerosol effects at the top of atmosphere (TOA, dFNET_toa) into direct and indirect effects, and surface albedo effects following the method of Ghan (2013) to understand the direct and indirect effects of aerosols. The total effects (sum of shortwave (SW) and longwave (LW) radiative effects) are shown in figures 2(a)–(d). The indirect effects of aerosols (figure 2(a)), caused by aerosol–cloud interactions and their impact on radiation, are most profound at the downstream Atlantic Ocean with the maximum of up to -10 W m^{-2}. The direct effects of aerosols (figure 2(b)), which are mainly due to the direct absorption and scattering of radiation by aerosols, are mostly confined to the regions where AOD are significantly increased. The contrast between all-sky (positive, figure 2(b)) and clear-sky (negative, figure 2(c)) direct effects in equatorial Atlantic indicates that clouds enhance the absorption by aerosols above the cloud top (Lu *et al* 2018) and it may be responsible to the large uncertainties in evaluating the total effects of aerosols (Boucher *et al* 2013). The effects of aerosols on surface albedo is shown in figure 2(d), which show profound responses in mid-to-high latitude, such as Europe and North America (dominated by the LW component, figure 2(f)). The significant change in LW surface albedo effects in Europe (figure 2(f)) is consistent with the surface warming shown in figure 1(d), suggesting that the warming surface emit much more LW radiation flux and enhance the radiative cooling effects at the TOA.

The above results indicate that the remote responses in total TOA radiative forcing are mainly from the surface albedo effects and surface temperature changes. However, the local radiative effects cannot in turn explain the significant remote surface temperature warming over Europe. Therefore, in the next subsection, we will explore how these remote responses of surface temperature anomalies are generated.

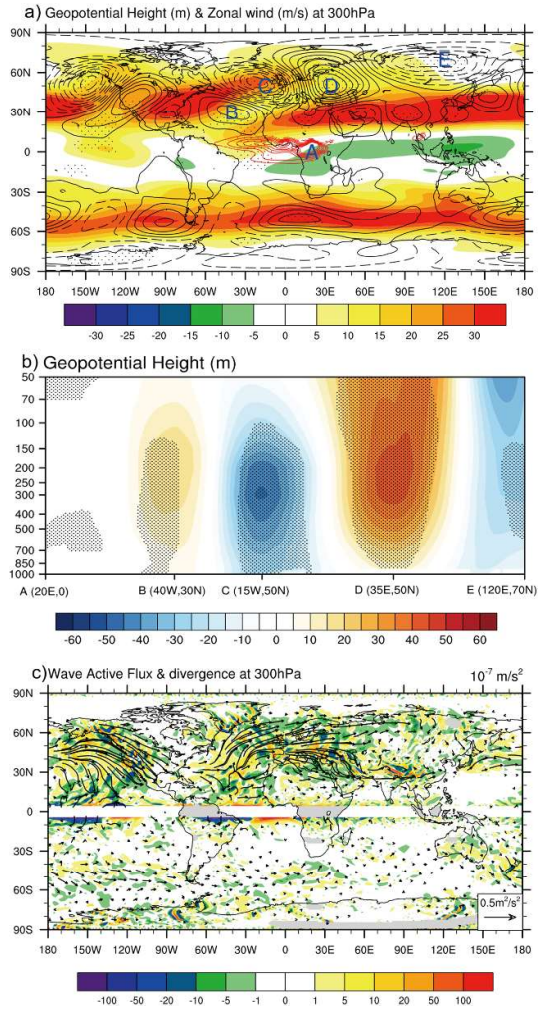

Figure 3. (a) The spatial distribution of zonal wind from noFire experiment (color shading, units: m s^{-2}) and geopotential height anomalies at 300 hPa due to fire aerosols (Fire experiment minus noFire experiment) (contour, at the internal of 3 m), red contours indicate the changes of aerosol optical depth (dAOD, only greater than 0.05 are shown); (b) the vertical cross section of geopotential height (color shading) along the centers (A to E) of the geopotential height anomalies in (a); (c) the spatial distribution of wave activity flux (vector, units: m^2 s^{-2}) and its divergence (color shading, units: 10^{-7} m s^{-2}). The geopotential height differences passing the 95% confidence level in (a) and (b) are dotted, and the wave activity flux and its divergence between 5° S and 5° N in (c) are masked out.

3.2. Fire aerosol-induced teleconnection patterns

As discussed in section 1, despite of the radiative effects, aerosols could have significant impacts on atmospheric circulations due to the nonhomogeneous spatial distribution radiative forcing. Thus, the circulation responses to African wildfire aerosols are analyzed in this section.

The zonal wind from the noFire experiment and the geopotential height anomalies at 300 hPa due to fire aerosols (Fire experiment minus noFire experiment) are presented in figure 3(a). Significant atmospheric responses to the wildfire appear over the mid-to-high latitudes of Northern Hemisphere with large magnitudes in North Atlantic, Europe, and Gulf of Alaska and the Pacific Northwest. The circulation changes are in well-organized wave-train patterns, in which the anomaly from North Atlantic across Europe to Siberia resembles the Eurasia teleconnection pattern (Liu *et al* 2014, Wang and Zhang 2015), and the anomaly over North America is more like a Pacific-North America (PNA) pattern (Wallace and Gutzler 1981, Leathers *et al* 1991) which ends at the southeast United States.

With the zonal wind at 300 hPa, we could further understand how such regional circulation changes are formed. The geopotential heights with

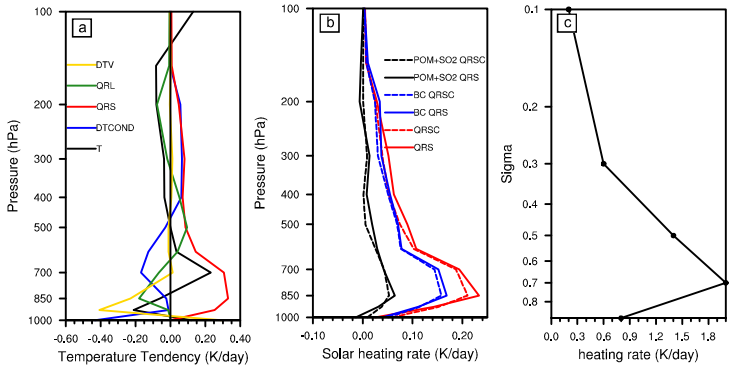

Figure 4. (a) the vertical profile of changes in temperature (T, units: K) and diabatic heating budgets (units: K d^{-1}) include solar heating rate (QRS), longwave heating rate (QRL), temperature tendency caused by moist processes (DTCOND), and temperature tendency from the diffusion (DTV) over the source regions (red contour in figure 3(a)). (b) The vertical profile of changes in solar heating rate (QRS) and that during clear sky (QRSC), BC effects on QRS and QRSC (derived from the difference between Fire and noBC experiments), and POM and SO_2 effects on QRS and QRSC (derived from the difference between noBC and noFire experiments) over the source regions. (c) The heating profile prescribed in the anomaly general circulation model (AGCM).

small magnitudes from the Middle East to East Asia corresponds with the westerly jet stream over Eurasia. At the exits of the Atlantic westerly jet and Asian westerly jet where locate the large horizontal gradients of the basic mean flow, the magnitude of the perturbation is amplified, resulting in significant geopotential height anomalies over North Atlantic, North Eurasia. These changes of circulations in the mid-to-high latitudes are barotropic in vertical (figure 3(b)).

The more than 2 K land surface warming over Europe locates between the cyclonic and anticyclonic anomalies of the circulation changes (figures 1(d) and 3(a)). Then, a nature question arised as to how does the atmospheric teleconnection induce the regional change in the surface air temperature, especially for the 2 K land surface warming over Europe? To answer this question, we diagnosed the relative contributions of each term in temperature equation: the temperature advection, the adiabatic heating, and the diabatic heating (see the supplementary material figure S2). The result shows that the advection term is the main contributor to the land surface warming over Europe, while the diabatic heating and adiabatic heating terms are much smaller than the advection term by two orders of magnitude. Therefore, the temperature advection that induced by the barotropical atmospheric teleconnections is mainly responsible for the remarkable Europe surface warming.

The wave activity flux defined in Takaya and Nakamura (2001) are calculated to identify the wave source and the propagation pathways of the Rossby waves. As shown in figure 3(c), strong wave activity fluxes are observed from the subtropical Atlantic to Europe, and from the gulf of Alaska to the Pacific Northwest, corresponding to the regions with robust circulation anomalies (figure 3(a)). For the wave train from the Middle East to East Asia, wave activity fluxes are relatively weak. Generally, there are two Rossby wave trains (figure 3(a)). One propagates northeastward to the northeast Atlantic, and further eastward to North Europe and Siberia. The other is a minor branch which propagates eastward, across Middle East to East Asia, and then further northward, bending equatorward over along the west coast of North America. For the minor branch, it can be found that the Asian westerly jet act as the waveguide for the wave propagation, which is consistent with previous studies (Lu *et al* 2002, Enomoto *et al* 2003). Two major divergent regions of wave activity flux can be found from figure 3(c), one is over subtropical North Atlantic, and the other is over North Pacific. Given that the circulation changes are all derived from the effects of the African wildfire, we infer that the subtropical North Atlantic (60°–30° W, 20°–40° N) located to the northwest of the wildfire aerosol source is the Rossby wave source region, and the anticyclone anomaly (figure 3(a)) is a direct tropical descending Rossby wave response to the atmospheric heating (Gill 1980) induced by the Africa wildfire aerosols.

3.3. Trigger of the teleconnections

From the wave activity flux analysis, we identified the Rossby wave source stems from the anticyclonic anomaly over the subtropical North Atlantic. Based on the Gill-type mechanism (Gill 1980), the anticyclonic anomaly is induced by the atmospheric heating. Thus, we first analyse the diabatic heating budget over the African aerosol source region, and then try to understand how the aerosols perturb the atmosphere and trigger the teleconnections in the mid-to-high latitudes.

Figure 4(a) illustrates the vertical profiles of air temperature (T), solar heating rate (QRS), longwave heating rate (QRL), moist process heating rate (DTCOND), and the temperature tendency from the diffusion (DTV) over equatorial African wildfire

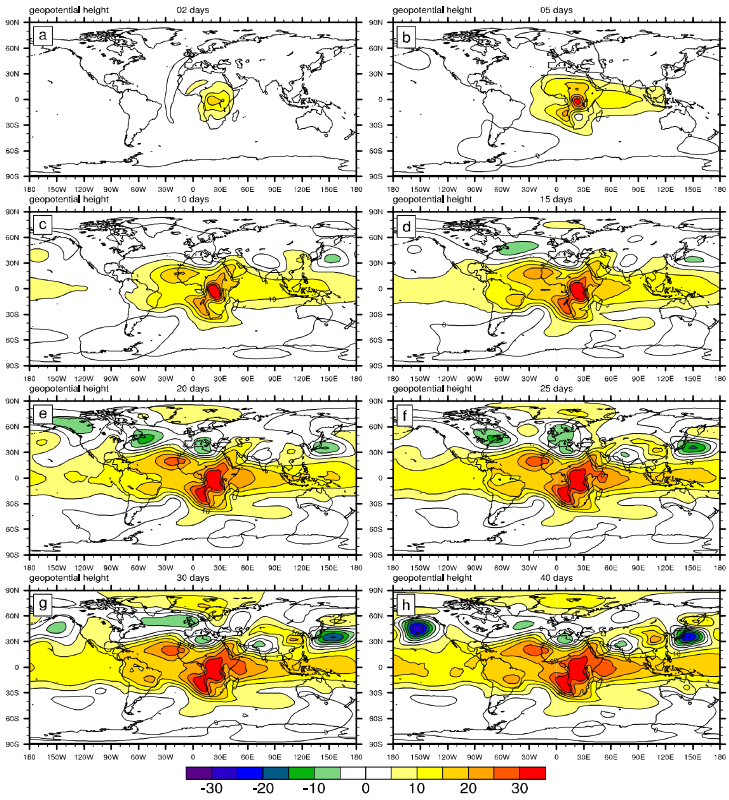

Figure 5. The temporal evolution of the 300 hPa geopotential height responses (units: m) with an idealized atmosphere heating (vertical profile is shown in figure 4(c)) added over equatorial Africa in AGCM.

regions. A peak warming of 0.2 K in T appears at 700 hPa. QRS shows significant increase below 600 hPa, while QRL has a negative peak at 850 hPa, and DTV is strongly negative near surface due to strong radiative forcing at surface. The DTCOND is negative below 500 hPa. In sum, for the atmospheric heating over the equatorial African wildfire region, QRS is the dominant contributor with its maximum at lower level troposphere.

As a strong absorbing aerosol, BC could enhance the absorption of solar radiation. It can be found that the enhanced QRS is mainly caused by the effect of BC (figure 4(b)). The magnitude of BC-induced solar heating rate can reach to 0.16 K d^{-1}, accounting for about 80% to the total aerosol effects on QRS. Thus, we conclude that the absorption of wildfire aerosols by BC mainly contributes the atmospheric heating over equatorial African wildfire region. In fact, Tosca *et al* (2013) and Jiang *et al* (2016) have also found the surface temperature warming over Europe as the response to direct and semi-direct effects of the aerosols (although the signals are less robust based on annual mean results). Such similarity provided us confidence on that the direct effect of wildfire aerosols (i.e. BC absorbing) induces the circulation anomalies and 2 K land surface warming over Europe in January.

To further validate that the teleconnections are triggered by the atmospheric heating induced by African wildfire aerosols. An intermediate AGCM was employed to study the formation mechanism of the teleconnection pattern. This model was based on the spectrum dry AGCM (Held and Suarez 1994) with five evenly distributed sigma levels from 0.9 to 0.1 and a horizontal resolution of around 2.88° × 2.88°. The climatological mean state is taken from that of the ensemble mean of the noFire experiments in January. A damping rate of 1 d^{-1} in the lowest level ($\sigma = 0.9$) and linearly decaying to 0.1 d^{-1} at the middle level ($\sigma = 0.7$) are taken as Rayleigh friction to apply to the momentum equations and to mimic the planetary boundary layer. Newtonian cooling with an e-folding time scale of 10 d is applied to the temperature equation at all model levels. The heating has a cosine-squared profile in an elliptical region over equatorial Africa in horizontal and the vertical profiles are given as in figure 4(c) with the maximum rate of 2 K d^{-1} at the level of $\sigma = 0.7$ to minic the atmospheric heating induced by the wildfire aerosols.

The time evolution of 300 hPa geopotential height response to the specified heating over the equatorial Africa are shown in figure 5. As expected, a northwestward-propagating Gill-type tropical Rossby wave duplet is induced over both sides of the equator to the west of the heating center. Meanwhile, a tropical Kelvin wave response is generated at the east of the heating center, propagating eastward. When the Rossby wave arrives around 30° N, it perturbs the westerly jet stream (figures 3(a) and 5(d)).

The westerly jet stream over North Atlantic leads to a northeastward propagation of the Rossby wave, forming the northern branch of the Rossby wave trains. The westerly jet stream over Eurasia acts as the waveguide and transports the perturbation to the East Asia, Pacific, and further to the west of the North America. The teleconnection patterns are quite steady after around 20 days integration. Compared to figure 3, the geopotential height anomalies over Europe, Pacific and North America from the idealized model are relatively weak. These discrepancies are possibly due to the southeastward shift of the anticyclone over the subtropical North Atlantic in the model, which limits the energy being transported northeastward by the westerly jet. Despite of such discrepancies, this idealized model simulation confirms that the atmospheric heating over equatorial Africa (induced by the wildfire aerosols) could generate the upper level anticyclone anomaly over the subtropical North Atlantic and further trigger the two Rossby wave trains in the mid-to-high latitudes of the Northern Hemisphere.

4. Conclusion and discussion

Using the global climate model CAM5, we evaluated the remote effects of wildfire aerosols emitted from equatorial Africa in January. Wildfire aerosols cause significantly radiative forcing over the source region and the downwind region over Atlantic, and further induce remote effects in the mid-to-high latitudes with a greater-than-2 K land surface warming in Europe. The remote response is imposed through atmospheric teleconnections in terms of Rossby wave trains. Through analyzing the wave activity flux and idealized AGCM simulation, we demonstrated that the equatorial African aerosol-induced low-level troposphere atmospheric heating could result in an anticyclonic anomaly over the subtropical North Atlantic. The anticyclonic anomaly perturbs westerly jet, and excites two Rossby wave trains. One Rossby wave train is along the great circle route via the northeast Atlantic and Europe to Siberia and the North Pacific, while the other is along the Asia jet stream eastward and northeastward with a shorter wave length toward the North Pacific, and then bending equatorward to Pacific Northwest. The budget analysis of the diabatic heating over the African aerosol source region indicates that the absorption of solar radiation by BC can contribute about 80% of the total changes of solar heating rate which plays the key role in stimulating the teleconnections.

Based on the Rossby wave theory, Rossby waves hardly escape from the tropics to the extratropics with a tropical easterly mean flow. Two possible mechanisms may explain our findings. One is that the vertical wind shear of the tropical mean flow can couple the baroclinic and barotropic Rossby wave modes; the baroclinic mode is trapped near the equator but the barotropic mode can emanate from the tropics to extratropics (Wang and Xie 1996, Xie and Wang 1996). The other one is that a southerly component in the basic easterly flow (a southerly conveyor) may transfer a Rossby wave source northward. Thus, a forcing embedded in the deep tropical easterlies may also excite a Rossby wave in the extratropical westerlies (Wang *et al* 2005).

Note that the strong negative radiative forcing over the equatorial Atlantic may further induce low frequency variability. Booth *et al* (2012) suggested that the anthropogenic aerosols may contribute to the multi-decadal variability of the North Atlantic SST. Amiri Farahani *et al* (2020) found the southern Africa fire aerosols could result in a La Nina-like SST response in a ocean coupled model. In this study, as we prescribed global SST, the strong cooling effects over the equatorial Atlantic are suppressed, and thus the Rossby wave trains we discussed in the present study are a fast response of the atmosphere. When an ocean model is coupled with the atmospheric model, the strong cooling effects on the Atlantic SST may induce low frequency variability which would combine the fast response of the atmosphere. We would not go any further for the coupled model in this study, but this may merit further investigations.

The waveguide effect of westerly jet in conveying the influences of tropical SST-forced diabatic heating to the globally climate variations (Li *et al* 2019) has been extensively investigated. For example, The Atlantic SST anomalies could excite eastward-propagated Rossby wave trains across the Eurasian continent throughout the year (Lu *et al* 2020, Zhu *et al* 2020), and the Rossby wave trains could be found on multiple timescales (e.g. from intraseasonal to interannual, and from decadal to multidecadal). In boreal summer, the Eurasian teleconnection pattern is associated with Atlantic SST (Lu *et al* 2002, Enomoto *et al* 2003, Sun *et al* 2015), while in boreal winter, an Africa–Asia teleconnection pattern embedded in the Asian jet is formed with the forcing of Atlantic SSTA (Sun *et al* 2017). The anomalous upper-level divergence/convergence associated with the SST warming/cooling contributes to Rossby wave source, whilst the westerly jet acts as a waveguide for the propagation of the Rossby wave, shaping the pathway of the teleconnections (Zhu and Li 2016). In the present study, we emphasis that besides the SST forcing, the heating effect of the African wildfire aerosols can also trigger these teleconnections with the help of the westerly jet in January.

Another point we would like to emphasize here is that although the total radiative forcing of wildfire aerosols (figure 2) (Jiang *et al* 2016) is cooling, what triggers the planetary Rossby waves and remote effects is the anomalous atmospheric heating induced by the absorbing aerosols. Thus, the existence of the absorbing aerosols may need more cautions and attentions. Furthermore, the 2 K land surface

warming over Europe would further enhance snow melting and reduce the snow cover and duration, leading to consequent ecological and socioeconomic impacts regionally and globally (Barnett *et al* 1988, Bamzai and Shukla 1999).

Data availability statement

The data that support the findings of this study are openly available at the following URL/DOI: www.globalfiredata.org.

Acknowledgments

This study was supported by the National Natural Science Foundation of China (Grant No. 42005155, the US Department of Energy (DOE)'s office of Science as part of the Regional and Global Climate Modeling Program (NSF-DOE-USDA EaSM2). The Pacific Northwest National Laboratory (PNNL) is operated for DOE by Battelle Memorial Institute under contract DE-AC05-76RL01830. The authors would like to acknowledge the use of computational resources at the NCAR-Wyoming Supercomputing Center and the National Energy Research Scientific Computing Center (NERSC) at Lawrence Berkeley National Laboratory. The anomaly model can be obtained from https://github.com/yanhp2009-git/Model/tree/v1.0.1 (doi:10.5281/zenodo.3947119).

ORCID iD

Zhiwei Zhu https://orcid.org/0000-0002-4885-1299

References

Allen R J and Sherwood S C 2011 The impact of natural versus anthropogenic aerosols on atmospheric circulation in the community atmosphere model *Clim. Dyn.* **36** 1959–78

Amiri-Farahani A, Allen R J, Li K, Nabat P and Westervelt D M 2020 A La Niña-like climate response to South African biomass burning aerosol in CESM simulations *J. Geophys. Res.* **125** e2019JD031832

Bamzai A S and Shukla J 1999 Relation between Eurasian snow cover, snow depth, and the Indian summer monsoon: an observational study *J. Clim.* **12** 3117–32

Barnett T P, Dümenil L, Schlese U and Roeckner E 1988 The effect of Eurasian snow cover on global climate *Science* **239** 504

Bollasina M A, Ming Y and Ramaswamy V 2013 Earlier onset of the Indian monsoon in the late twentieth century: the role of anthropogenic aerosol *Geophys. Res. Lett.* **40** 3715–20

Booth B B B, Dunstone N J, Halloran P R, Andrews T and Bellouin N 2012 Aerosols implicated as a prime driver of twentieth-century North Atlantic climate variability *Nature* **484** 228–32

Boucher O, Randall D, Artaxo P, Bretherton C, Feingold G, Forster P, Kerminen V, Kondo Y, Liao H and Lohmann U 2013 Clouds and Aerosols: In Climate Change 2013: The Physical Science Basis Contribution of Working Group I to the Fifth Assessment Report of the Intergovernmental Panel on Climate Change (Cambridge: Cambridge University Press)

Chen J P, Chen I J and Tsai I C 2016 Dynamic feedback of aerosol effects on the East Asian summer monsoon *J. Clim.* **29** 6137–49

Enomoto T, Hoskins B and Matsuda Y 2003 The formation mechanism of the Bonin high in August *Q. J. R. Meteorol. Soc.* **129** 157–78

Ganguly D, Rasch P J, Wang H L and Yoon J H 2012 Climate response of the South Asian monsoon system to anthropogenic aerosols *J. Geophys. Res.* **117** D13209

Ghan S J 2013 Technical note: estimating aerosol effects on cloud radiative forcing *Atmos. Chem. Phys.* **13** 9971–4

Giglio L, Randerson J T and Werf G R 2013 Analysis of daily, monthly, and annual burned area using the fourth-generation global fire emissions database (GFED4) *J. Geophys. Res.* **118** 317–28

Gill A E 1980 Some simple solutions for heat-induced tropical circulation *Q. J. R. Meteorol. Soc.* **106** 447–62

Giorgi F, Bi X Q and Qian Y 2002 Direct radiative forcing and regional climatic effects of anthropogenic aerosols over East Asia: a regional coupled climate-chemistry/aerosol model study *J. Geophys. Res.* **107** 4439

Giorgi F, Bi X Q and Qian Y 2003 Indirect vs. direct effects of anthropogenic sulfate on the climate of East Asia as simulated with a regional coupled climate-chemistry/aerosol model *Clim. Change* **58** 345–76

Global Fire Emissions Database

Held I M and Suarez M J 1994 A proposal for the intercomparison of the dynamical cores of atmospheric general circulation models *Bull. Am. Meteorol. Soc.* **75** 1825–30

Jacob D J 1999 Introduction to Atmospheric Chemistry (Princeton, NJ: Princeton University Press)

Jiang Y Q, Liu X H, Yang X Q and Wang M H 2013 A numerical study of the effect of different aerosol types on East Asian summer clouds and precipitation *Atmos. Environ.* **70** 51–63

Jiang Y, Lu Z, Liu X, Qian Y, Zhang K, Wang Y and Yang X Q 2016 Impacts of global open-fire aerosols on direct radiative, cloud and surface-albedo effects simulated with CAM5 *Atmos. Chem. Phys.* **16** 14805–24

Kim M K, Lau W K M, Chin M, Kim K M, Sud Y C and Walker G K 2006 Atmospheric teleconnection over Eurasia induced by aerosol radiative forcing during boreal spring *J. Clim.* **19** 4700–18

Lamarque J F *et al* 2010 Historical (1850–2000) gridded anthropogenic and biomass burning emissions of reactive gases and aerosols: methodology and application *Atmos. Chem. Phys.* **10** 7017–39

Lau K M, Kim M K and Kim K M 2006 Asian summer monsoon anomalies induced by aerosol direct forcing: the role of the Tibetan Plateau *Clim. Dyn.* **26** 855–64

Leathers D J, Yarnal B and Palecki M A 1991 The Pacific/North American teleconnection pattern and United States climate. Part I: regional temperature and precipitation associations *J. Clim.* **4** 517–28

Li J, Zheng F, Sun C, Feng J and Wang J 2019 Pathways of influence of the Northern Hemisphere mid–high latitudes on East Asian climate: a review *Adv. Atmos. Sci.* **36** 902–21

Li Z *et al* 2016 Aerosol and monsoon climate interactions over Asia *Rev. Geophys.* **54** 866–929

Liu X, Ma P L, Wang H, Tilmes S, Singh B, Easter R C, Ghan S J and Rasch P J 2016 Description and evaluation of a new four-mode version of the Modal Aerosol Module (MAM4) within version 5.3 of the Community Atmosphere Model *Geosci. Model Dev.* **9** 505–22

Liu Y, Goodrick S and Heilman W 2014 Wildland fire emissions, carbon, and climate: wildfire–climate interactions *For. Ecol. Manage.* **317** 80–96

Liu Y, Sun J R and Yang B 2009 The effects of black carbon and sulphate aerosols in China regions on East Asia monsoons *Tellus* B **61** 642–56

Lou S, Yang Y, Wang H, Smith S J, Qian Y and Rasch P J 2019 Black carbon amplifies haze over the North China plain by weakening the East Asian Winter Monsoon *Geophys. Res. Lett.* **46** 452–60

Lu R, Oh J and Kim B 2002 A teleconnection pattern in upper-level meridional wind over the North African and Eurasian continent in summer *Tellus* **54A** 44–55

Lu R, Zhu Z, Li T and Zhang H 2020 Interannual and interdecadal variabilities of spring rainfall over northeast China and their associated sea surface temperature anomaly forcings *J. Clim.* **33** 1423–35

Lu Z, Liu X H, Zhang Z B, Zhao C, Meyer K, Rajapakshe C, Wu C L, Yang Z F and Penner J E 2018 Biomass smoke from southern Africa can significantly enhance the brightness of stratocumulus over the southeastern Atlantic Ocean *Proc. Natl Acad. Sci. USA* **115** 2924–9

Meehl G A, Arblaster J M and Collins W D 2008 Effects of black carbon aerosols on the Indian monsoon *J. Clim.* **21** 2869–82

Ming Y, Ramaswamy V and Chen G 2011 A model investigation of aerosol-induced changes in boreal winter extratropical circulation *J. Atmos. Sci.* **24** 6077–91

Morrison H, Gettelman A, Morrison H and Ghan S J 2008 A new two-moment bulk stratiform cloud microphysics scheme in the community atmosphere model, version 3 (CAM3). Part I: description and numerical tests *J. Clim.* **21** 3660–79

Neale R B, Chen C C, Gettelman A, Lauritzen P H, Park S, Williamson D L, Conley A J, Garcia R, Kinnison D and Lamarque J F 2010. Description of the NCAR community atmosphere model (CAM 5.0) *NCAR Tech. Note NCAR/TN-486+ STR*

Qian Y, Flanner M G, Leung L R and Wang W 2011 Sensitivity studies on the impacts of Tibetan Plateau snowpack pollution on the Asian hydrological cycle and monsoon climate *Atmos. Chem. Phys.* **11** 1929–48

Qian Y, Giorgi F, Huang Y, Chameides W and Luo C 2001 Regional simulation of anthropogenic sulfur over East Asia and its sensitivity to model parameters *Tellus* B **53** 171–91

Ramanathan V and Carmichael G 2008 Global and regional climate changes due to black carbon *Nat. Geosci.* **1** 221–7

Rodwell M J and Jung T 2008 Understanding the local and global impacts of model physics changes: an aerosol example *Q. J. R. Meteorol. Soc.* **134** 1479–97

Song F F, Zhou T J and Qian Y 2014 Responses of East Asian summer monsoon to natural and anthropogenic forcings in the 17 latest CMIP5 models *Geophys. Res. Lett.* **41** 596–603

Sun C, Li J, Ding R and Jin Z 2017 Cold season Africa–Asia multidecadal teleconnection pattern and its relation to the Atlantic multidecadal variability *Clim. Dyn.* **48** 3903–18

Sun C, Li J and Zhao S 2015 Remote influence of Atlantic multidecadal variability on Siberian warm season precipitation *Sci. Rep.* **5** 16853

Takaya K and Nakamura H 2001 A formulation of a phase-independent wave-activity flux for stationary and migratory quasigeostrophic eddies on a zonally varying basic flow *J. Atmos. Sci.* **58** 608–27

Tosca M G, Randerson J T and Zender C S 2013 Global impact of smoke aerosols from landscape fires on climate and the Hadley circulation *Atmos. Chem. Phys.* **13** 5227–41

van der Werf G R, Randerson J T, Giglio L, van Leeuwen T T, Chen Y, Rogers B M, Mu M, van Marle M J, Morton D C, Collatz G J, Yokelson R J and Kasibhatla P S 2017 Global fire emissions estimates during 1997–2016 *Earth Syst. Sci. Data* **9** 697–720

Wallace J M and Gutzler D S 1981 Teleconnections in the geopotential height field during the Northern Hemisphere Winter *Mon. Weather Rev.* **109** 784–812

Wang B and Xie X 1996 Low-frequency equatorial waves in vertically sheared zonal flow. Part i: stable waves *J. Atmos. Sci.* **53** 449–67

Wang N and Zhang Y 2015 Evolution of Eurasian teleconnection pattern and its relationship to climate anomalies in China *Clim. Dyn.* **44** 1017–28

Wang Z, Chang C P, Wang B and Jin F F 2005 Teleconnections from tropics to northern extratropics through a southerly conveyor *J. Atmos. Sci.* **62** 4057–70

Xie X and Wang B 1996 Low-frequency equatorial waves in vertically sheared zonal flow. Part II: unstable waves *J. Atmos. Sci.* **53** 3589–605

Yang J, Wang W, Chen G, Bao Q, Qi X and Zhou S 2018 Intraseasonal variation of the black carbon aerosol concentration and its impact on atmospheric circulation over the southeastern Tibetan Plateau *J. Geophys. Res.* **123** 881–94

Yasunari T J, Koster R D, Lau W K M and Kim K M 2015 Impact of snow darkening via dust, black carbon, and organic carbon on boreal spring climate in the Earth system *J. Geophys. Res.* **120** 5485–503

Zhang H *et al* 2012 Simulation of direct radiative forcing of aerosols and their effects on East Asian climate using an interactive AGCM-aerosol coupled system *Clim. Dyn.* **38** 1675–93

Zhou S, Yang J, Wang W, Zhao C, Gong D and Shi P 2020 An observational study of the effect of aerosols on diurnal variation of heavy rainfall and associated clouds over Beijing-Tianjin-Hebei *Atmos. Chem. Phys.* **20** 1–19

Zhu Z and Li T 2016 A new paradigm for Continental U.S. summer rainfall variability: Asia–North America teleconnection *J. Clim.* **29** 7313–27

Zhu Z, Li T and He J 2014 Out-of-phase relationship between boreal spring and summer decadal rainfall changes in southern China *J. Clim.* **27** 1083–99

Zhu Z, Lu R, Yan H, Li W, Li T and He J 2020 The dynamic origin of the interannual variability of West China Autumn Rainfall *J. Clim.* **33** 9643–52

Supplementary information for:

Tropical African wildfire aerosols Trigger Teleconnections in the mid-high latitude of Northern Hemisphere in January

Huiping Yan[1], Zhiwei Zhu[1], Bin Wang[2,1], Kai Zhang[3], Jingjia Luo[1], Yun Qian[3], Yiquan Jiang[4]

1 School of Atmospheric Sciences, Nanjing University of Information Science and Technology, Nanjing, China

2 Department of Meteorology, University of Hawaii at Manoa, Honolulu, Hawaii, USA

3 Pacific Northwest National Laboratory, Richland, Washington, USA

4 School of Atmospheric Sciences, Nanjing University, Nanjing, China

*Corresponding author:

Zhiwei Zhu, Nanjing University of Information Science and Technology, Ningliu Road 219, Meteorology Bldg. Jiangsu 210044, China. E-mail: zwz@nuist.edu.cn.

This file includes:

Supplementary figures S1-S2

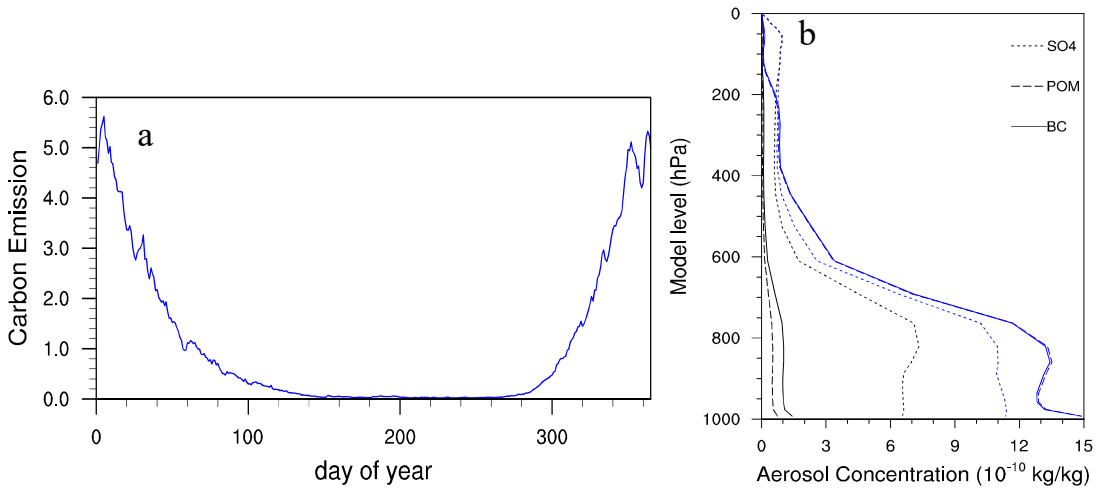

Figure S1. (a) the climatology daily evolution of carbon emissions (units: Tg C) of North Africa wildfire and (b) the vertical profiles of black carbon (BC), primary organic carbon (POM), and SO4 concentration in January averaged over the African fire region from CAM5 simulations (black line for noFire experiment, blue line for Fire experiment) (units: 10^{-10} kg/kg, POM was scaled by 10, and SO4 was scaled by 2).

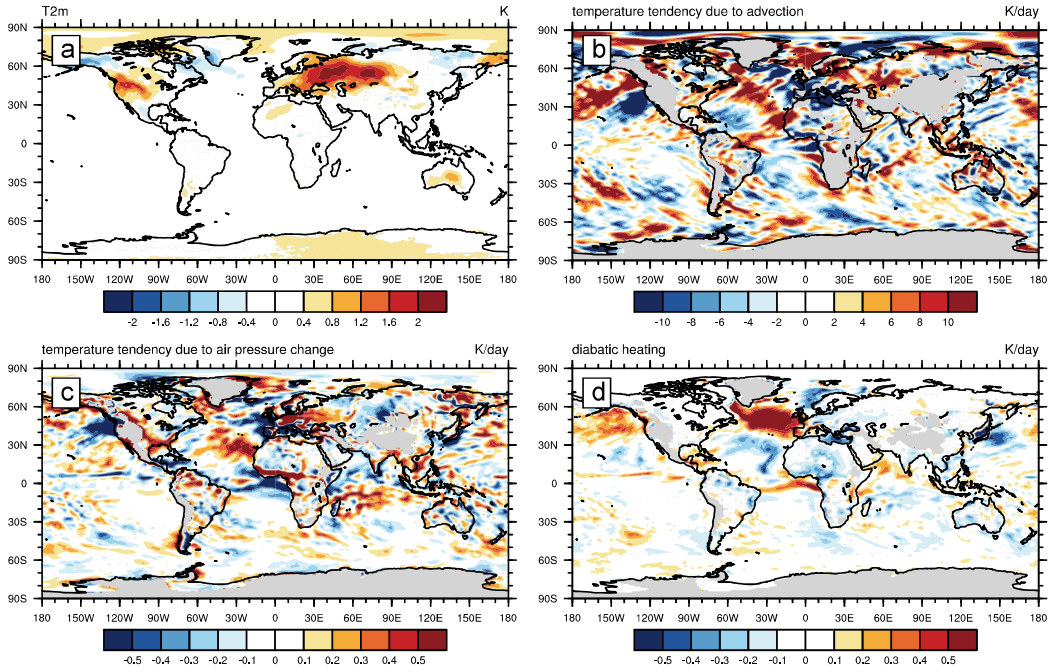

Figure S2. The differences of (a) the surface air temperature from December to January (units: K) between Fire and noFire experiments, (b) the temperature tendency due to the temperature advection (only including horizontal and vertical terms) (units: K/day), (c) the temperature tendency induced by the air pressure change (units: K/day), and (d) the diabatic heating rate (units: K/day).

The temperature equation is

$$\frac{\partial T}{\partial t} = -\vec{V} \cdot \nabla T + \frac{\alpha\omega}{c_p} + \frac{\dot{Q}}{c_p} \quad (1)$$

Specially, T is temperature, $\vec{V}$ is 3-d velocity vector, α is the reciprocal of air density, ω is pressure velocity, c_p is the air specific volume, and $\dot{Q}$ is the diabatic heating. $\frac{\alpha\omega}{c_p}$ is the adiabatic heating term, while $\frac{\dot{Q}}{c_p}$ is the diabatic heating. Some modifications were made on the equation (1) before we made the calculations.

$$\frac{\partial T}{\partial t} = -\vec{V} \cdot \nabla T + \frac{\alpha\omega}{c_p} + \frac{\dot{Q}}{c_p} = -\nabla \cdot \vec{V}T - T\nabla \cdot \vec{V} + \frac{R\omega T}{Pc_p} + \frac{\dot{Q}}{c_p} \quad (2)$$

Within pressure coordinate, we have $\nabla \cdot \vec{V} = 0$, thus the equation (2) can be written as below

$$\frac{\partial T}{\partial t} = -\left(\frac{\partial uT}{\partial x} + \frac{\partial vT}{\partial y} + \frac{\partial \omega T}{\partial p}\right) + \frac{R\omega T}{Pc_p} + \frac{\dot{Q}}{c_p} \quad (3)$$

The diabatic heating rates include four terms: shortwave heating rate (QRS), longwave heating rate (QRL), moisture heat release (DTCOND), and vertical diffuse (DTV), which were outputted in CAM5 history files. And vT and ωT were also in CAM5 history files. Since the meridional and vertical gradient of temperature are much greater than the zonal gradient of temperature, we ignored the term of $\frac{\partial uT}{\partial x}$ when calculating the advection terms.